THE JOURNAL OF PHYSICAL CHEMISTRY C
A JOURNAL OF THE AMERICAN CHEMICAL SOCIETY



pubs.acs.org/JPCC
Article

# $Fe_3O_4$@Fe Core–Shell Okara-Derived Activated Carbon for Superior Polysulfide Control in Lithium–Sulfur Batteries

Ka Chun Li, Feng Shi, Xuanming Chen, Zeyuan Di, Moyu Hu, Long Bun Sin, Chi Ho Wong, Leung Yuk Frank Lam,* and Xijun Hu*

Cite This: J. Phys. Chem. C 2025, 129, 15507–15517



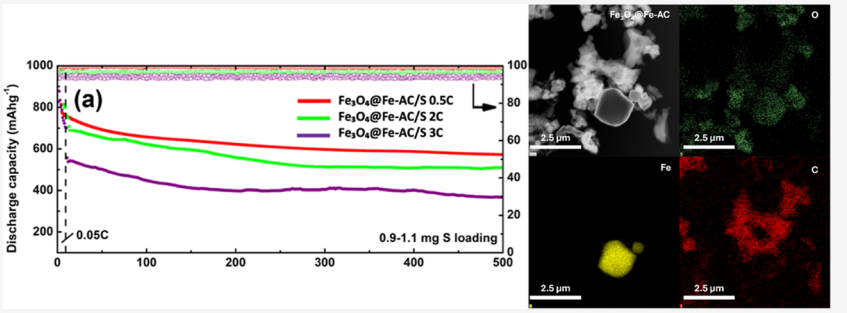


**ABSTRACT:** Lithium–sulfur (Li–S) batteries offer high energy density but suffer from a polysulfide shuttle effect, leading to capacity fading and poor cycling stability. To address this, the $Fe_3O_4$@Fe core–shell Okara-derived activated carbon ($Fe_3O_4$@Fe-AC) using a sustainable and scalable approach with okara, a soybean residue, as the carbon precursor was developed. Electrochemical tests demonstrate that $Fe_3O_4$@Fe-AC/S cathodes exhibit superior cyclic stability, achieving an initial discharge capacity of 755 mAh/g at 0.5C and retaining 572 mAh/g after 500 cycles, with an ultralow capacity decay rate of 0.050% per cycle. At a high rate of 3C, the battery delivers an initial capacity of 557 mAh/g and retains a capacity of 367 mAh/g after 500 cycles, highlighting its excellent rate performance and low polarization potential. This composite enhances battery performance by integrating high-surface-area activated carbon for physical polysulfide adsorption, $Fe_3O_4$ for dipole–dipole interactions, and metallic Fe for catalytic LiPS conversion. With its high electrochemical performance, cost-effective synthesis, and sustainable precursor, $Fe_3O_4$@Fe-AC represents a promising material for practical Li–S battery applications.

## INTRODUCTION

Soymilk is one of the most popular beverages in Hong Kong. To meet market demands, large quantities of soybeans are processed daily for soymilk production, generating significant amounts of okara as a byproduct. Annually, a significant amount of okara in ktons is produced through soymilk production processes. Most of this okara is currently repurposed as fertilizer through a food waste collection scheme supported by the government. Beyond its use as fertilizer, efforts are being made to explore alternative applications for this substantial byproduct, aiming to achieve a "zero manufacturing waste footprint". One area of focus is its potential use in the battery industry. With the increasing demand for mobile devices, including cell phones and electric vehicles, there is a pressing need for batteries with a higher energy density. Lithium–sulfur (Li–S) batteries are particularly promising in this regard, offering a theoretical energy density of 2508.5 Wh/kg and a capacity of 1672 mAh/g. The affordability of sulfur further enhances its appeal. However, the commercialization of Li–S batteries faces several challenges. These include sulfur's insulating properties, the volume expansion of the cathode after discharge, and the problematic "polysulfide shuttle" effect. This effect arises from the release of lithium polysulfides (LiPS) from the cathode into organic-based electrolytes. LiPS molecules can migrate from the cathode to the anode through the separator, forming an insulating layer on the anode's active surface and hampering the battery performance.

To address the shuttle effect, various materials have been employed as cathode components. Advanced sulfur hosts are designed to confine LiPS within the cathode, preventing them from reaching the lithium anode. Carbon-based materials such as nanoarchitectured graphene,[1] reduced graphene oxide,[2] carbon nanotubes,[3] have proven effective due to their high

Received: April 16, 2025
Revised: August 11, 2025
Accepted: August 12, 2025
Published: August 20, 2025

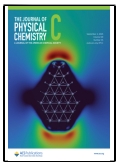







https://doi.org/10.1021/acs.jpcc.5c02606
J. Phys. Chem. C 2025, 129, 15507–15517

electrical conductivity and porosity, which promote sulfur utilization and physically adsorb LiPS.

Another well-known type of carbon, activated carbon, has also been extensively investigated as an cathode material for lithium−sulfur batteries due to its high-surface area and porous structure, which facilitate the physical adsorption of LiPS. However, this mode of adsorption is relatively weak and fails to effectively suppress the well-documented shuttle effect caused by the dissolution and migration of soluble LiPS during battery operation. To address this limitation, materials capable of strong chemical adsorption have been explored. Among these, metal oxides such as NiO,[4] MnO,[5] $Al_2O_3$,[6] $Fe_2O_3$,[7] and $TiO_2$[8−17] have attracted significant attention because their strong positive charge, which results from the presence of highly electronegative elements such as oxygen or nitrogen, enables them to form dipole−dipole interactions with negatively charged lithium LiPS.

Despite their superior chemical adsorption properties, metal oxides suffer from poor electrical conductivity. The incorporation of nonconductive metal oxides within the cathode increases internal resistance, which reduces overall battery efficiency. In addition to adsorption, the rapid conversion of LiPS into $Li_2S_2/Li_2S$ is crucial for mitigating the shuttle effect. Long-chain LiPS exhibits lower polarity and greater solubility in organic electrolytes, leading to increased dissolution and further exacerbation of the shuttle effect. Although catalytic strategies employing metallic iron have been explored to promote this conversion, the susceptibility of iron to oxidation and its relatively small-surface area present significant challenges.

To overcome these drawbacks, a synergistic approach that integrates carbon-based materials with metals has been proposed. In such a composite, the carbon matrix provides high-surface area with low polarity that facilitates the adsorption of LiPS, while the presence of iron compounds enhances the adsorption of LiPS and catalyzes their conversion to shorter-chain species. Previous studies on materials such as Graphitic C/$Fe_3C$,[18] $Fe_3C$@NCNT,[19] FeSA−CN,[20] and Fe-PNC[21] have demonstrated the effectiveness of this approach. However, the relatively low-surface areas of these materials and the complexity of their synthesis processes have hindered their commercial viability.

In this study, molecular dynamics (MD) simulations were conducted to assess the interactions between various metal oxides and LiPS. The simulations revealed that $Fe_3O_4$ exhibited interaction performance comparable to $TiO_2$, but $Fe_3O_4$ was ultimately chosen for this project due to its lower cost and the ease with which its precursors can be prepared in aqueous form for further reactions. Then, a scalable and sustainable method for fabricating $Fe_3O_4$@Fe core−shell activated carbon ($Fe_3O_4$@Fe-AC) is proposed. The material is synthesized using okara, a soybean residue generated from soy beverage production, as the carbon precursor by incorporating an iron compound into the precursor material and subjecting the mixture to high-temperature calcination. The resulting composite consists of three key components, each contributing to LiPS regulation. The activated carbon component provides a large-surface area, facilitating the physical adsorption of LiPS. The surface $Fe_3O_4$ component introduces dipole−dipole interactions, enhancing LiPS adsorption. Meanwhile, the metallic Fe sites serve as active catalytic centers, promoting the conversion of LiPS.[18] Additionally, the intrinsic magnetism of $Fe_3O_4$@Fe-AC enables the convenient separation and recovery of the material after use, further enhancing the recyclability of the system. This characteristic contributes to the overall sustainability of the process by reducing waste and improving material reuse. This dual-function material not only presents an effective strategy for mitigating the shuttle effect in lithium−sulfur batteries but also offers an environmentally sustainable solution by utilizing industrial byproducts. The combination of a scalable synthesis route, enhanced recyclability, and improved battery performance demonstrates significant potential for large-scale production and broader commercial applications.

## EXPERIMENTAL SECTION

**Synthesis of Sulfur Host ($Fe_3O_4$@Fe-AC and SYBAC).** The soybean waste collected was thoroughly dried in an oven set at 100 °C. First, 30 g of the dried soybean waste was combined with 3.3 g of iron(III) chloride hexahydrate, 6.8 g of iron(II) sulfate heptahydrate, and 200 mL of deionized (DDI) water. The mixture underwent magnetic stirring for a period of 3 h. Then, the soybean waste was separated from the mixture by using simple filtration. The filtered soybean waste was subsequently mixed with 60 g of KOH and 100 mL of water, yielding a black mixture. This mixture was then transferred to an oven set at 120 °C for drying. Once dried, the black mixture was put in a tube furnace for pyrolysis at 700 °C with a ramping rate of 5 K/min for 1 h, under ultrahigh purity nitrogen (UHP $N_2$) conditions. Finally, the resultant pyrolyzed product was washed with DDI water and dried in an oven set at 100 °C to obtain the $Fe_3O_4$@Fe-AC. SYBAC, which is the activated carbon without iron doping, was synthesized with a similar method without addition of iron salts solution.

**Synthesis of Sulfur Host/S Composites.** The sulfur host and sulfur composites were synthesized by using the melt-diffusion technique. For example, the $Fe_3O_4$@Fe-AC composite was thoroughly blended with sublimated sulfur in a weight ratio of 1:3 using ball milling for 4 h. This mixture was then transferred to a quartz boat and placed inside a tube furnace. The temperature was gradually raised to 155 °C at a rate of 3 K/min and sustained for 12 h in an argon atmosphere. Post heat treatment, the sample was pulverized into a fine powder through ball milling. For comparative performance analysis, the Super P/S composites were fabricated using an identical procedure. SYBAC/S composites and Super P/S composite were prepared by the same method with $Fe_3O_4$@Fe-AC/S composites.

**Polysulfide Adsorption Test.** From the literature,[22−24] an adsorption experiment targeting LiPS was carried out to assess the adsorption efficiency of the materials. To formulate the $4 \times 10^{-3}$ M $Li_2S_6$ solution, stoichiometric quantities of sublimated sulfur and lithium sulfide ($Li_2S$) were combined in a molar ratio of 5:1. This mixture was then dissolved in a DME/DOL solution (v/v = 1:1) and magnetically stirred for 48 h, yielding a deep orange solution. Following this, 30 mg of the sulfur hosts ($Fe_3O_4$@Fe-AC, SYBAC, and Super P) was introduced to a transparent container, into which 2.5 mL of the $Li_2S_6$ solution was added. The mixture was shaken briefly for 5 min and subsequently left to stabilize in a glovebox to avoid air exposure.

The morphologies of the samples were examined using scanning electron microscopy (SEM, JEOL-6390F) and transmission electron microscopy (TEM, JEM 2010F). The samples' ordered structures were characterized by X-ray diffraction (XRD, PW1830) and nitrogen ($N_2$) adsorption−


https://doi.org/10.1021/acs.jpcc.5c02606
J. Phys. Chem. C 2025, 129, 15507−15517

desorption isotherms (MicrotracBEL BELSORP MAX G). Additionally, the chemical composition of the samples was determined through X-ray photoelectron spectroscopy (XPS, Physical Electronics 5600) with a monochromatic Al K$\alpha$ source.

**Symmetrical Cell Test.** Symmetric batteries were assembled following the same procedure as for lithium−sulfur batteries. Both the working and counter electrodes consisted of identical active materials ($Fe_3O_4$@Fe-AC). A total of 40 $\mu$L of a 0.5 M $Li_2S_6$ solution was added as the electrolyte. The assembled cells were configured as CR2032 coin cells, utilizing a Celgard 2400 separator. For comparison, symmetric batteries incorporating SYBAC electrodes and the same electrolyte solution were also fabricated and evaluated. Cyclic voltammetry (CV) measurements were conducted using an electrochemical workstation within a voltage range of −1.0−1.0 V at a scan rate of 10 mV $s^{-1}$.

**Electrochemical Measurements.** Sulfur composites were combined with conductive multiwalled carbon nanotubes (MWCNT) and poly(vinylidene fluoride) (PVDF) in a weight ratio of 7:2:1 through ball milling. To this mixture, a *N*-methyl-2-pyrrolidone (NMP) solution was added, yielding a homogeneous, toothpaste-like slurry. Using the doctor blade technique, this slurry was uniformly spread onto the aluminum foil. After drying the coated foil overnight at 60 °C in a vacuum oven, it was cut into 12 mm diameter discs, which were designated as cathodes for the lithium−sulfur coin cells. Inside an argon-filled glovebox, the cells were assembled, incorporating a Celgard 2325 separator and a lithium foil anode. The electrolyte was formulated by blending 1,3-dioxolane and 1,2-dimethoxyethane at a 1:1 volume ratio, enriched with 1 M lithium bis(trifluoromethanesulfone)imide and 0.1 M $LiNO_3$. Each cell was infused with roughly 30 $\mu$L of this electrolyte. For performance evaluation, the assembled batteries underwent galvanostatic analysis at varying current densities between 1.7 and 2.8 V using a CT4008T cell test instrument (NEWARE, China). Additionally, cyclic voltammetry (CV) scans were performed on the batteries within a voltage window of 1.7−2.8 V using an electrochemical workstation (CH instrument, China). The galvanostatic intermittent titration test (GITT) performed at 0.05C with 20 min discharge/charge and 2 h OCV rest.[25] Cyclic voltammetry (CV) scanning of the assembled batteries was also conducted using an electrochemical workstation (CH Instrument, China) in the voltage range of 1.7−2.8 V.

**Molecular Dynamics (MD) Simulation.** All molecular dynamics simulations were conducted using the large atomic/molecular parallel simulator (LAMMPS)[26] To simulate the morphology of $Fe_3O_4$ in realistic environments, this study utilized the Forcite module in Materials Studio to construct nano $Fe_3O_4$ clusters with a diameter of 30 Å, comprising 582 Fe atoms, 776 O atoms. The $Li_2S_8$ was constructed by the Amorphous Cell module. Subsequently, the particle were supported onto the graphene, with dimensions of 68.17 Å × 78.72 Å × 11.90 Å, consisting of a total of 8192C atoms. Periodic boundary conditions were applied in the *X*, *Y*, and *Z* directions. The Tersoff potential was utilized for interactions between $Fe_3O_4$.[27] For the interlayer and intralayer interactions within the graphene, the AIREBO potential was employed.[28] The interactions of $Li_2S_8$ are uses as $P_{cff}$.[29] The LJ potential function was applied to describe the interactions between the $Fe_3O_4$ and the substrate, the $Li_2S_8$ and the substrate, and the $Li_2S_8$ and the substrate. The specific form and parameters of the potentials can be found in the Supporting Information.

**Density Functional Theory (DFT) Calculation.** The calculations for this study were executed using CASTEP software, a widely recognized tool for performing first-principles quantum mechanical calculations. In our study, the generalized gradient approximation (GGA) was employed within the Perdew−Burke−Ernzerhof (PBE) functional framework,[30,31] which is known for its accuracy in handling exchange−correlation effects in density functional theory (DFT) calculations. To ensure reliable results, ultrasoft pseudopotentials were utilized, enhancing the efficiency of the calculations. Specifically, for the $Fe_3O_4$ system, a vacuum distance exceeding 10 Å was meticulously maintained to prevent any spurious interactions between consecutive slabs,[32] which could otherwise compromise the accuracy of the results. The cutoff energy for the projector augmented plane-wave basis set was carefully set at 450 eV,[33,34] a value that has been validated in previous studies. Furthermore, the threshold for self-consistent field (SCF) iterations was rigorously defined at $1 \times 10^{-6}$ eV/atom,[35,36] ensuring a high degree of precision in the convergence of electronic states. The adsorption energy ($E_a$) for $Li_2S_4$ on the $Fe_3O_4$ surface was determined using the equation $E_{ads} = E_{total} - E_{Li_2S_4} - E_{surf}$, where $E_{total}$ represents the total energy of the system with adsorbed $Li_2S_4$, $E_{Li_2S_4}$ is the energy of $Li_2S_4$ under vacuum, and $E_{surf}$ corresponds to the energy of the optimized clean $Fe_3O_4$ surface slab.[13]

## RESULTS AND DISCUSSION

**LiPS Adsorption Simulation.** The initial configuration of the $Fe_3O_4$ particles was optimized by using an annealing method. This annealing process involved heating the $Fe_3O_4$ particles from 300 to 1300 K over a period of 500 ps, maintaining the temperature at 1300 K for 50 ps, and then cooling back to 300 K within 50 ps. Throughout this process, the $Fe_3O_4$ particles were maintained in the *NVT* ensemble to manage temperature variations, with temperature control achieved by using a Nose−Hoover thermostat. To prevent significant deformation of the carbon substrate at high temperatures, which could interfere with structural analysis, four layers of graphene were kept fixed. Atomic trajectories during the simulation were visualized using OVITO software.[37] The annealing process is depicted in Figure 1a.

As shown in Figure 1b, 30 $Li_2S_8$ molecules were introduced above the $Fe_3O_4$ particles to evaluate their adsorption performance. Initially, the $Li_2S_8$ molecules were positionally constrained while the system was heated and equilibrated at 300 K. After equilibration, the constraints on the $Li_2S_8$ molecules were released, allowing free movement to accurately simulate the adsorption process. As depicted in Figure 1c, after 3 ns, the $Li_2S_8$ molecules were adsorbed only on the surface of $Fe_3O_4$, with no adsorption observed on the carbon substrate.

Similar simulation processes were conducted for other common metal oxides, including $TiO_2$, $Al_2O_3$, and MnO, as visualized in Figure 2. The diameter of all oxide particles is also maintained at 3 nm, and the force field parameters can be found in the Supporting Information. The number of $Li_2S_8$ molecules adsorbed on each metal oxide surface was counted to assess and compare their adsorption capabilities. The results of these simulations are summarized in Table 1.

The results demonstrate that $TiO_2$ exhibited the highest $Li_2S_8$ adsorption capacity, successfully adsorbing 29 of 30 $Li_2S_8$



https://doi.org/10.1021/acs.jpcc.5c02606
J. Phys. Chem. C 2025, 129, 15507−15517

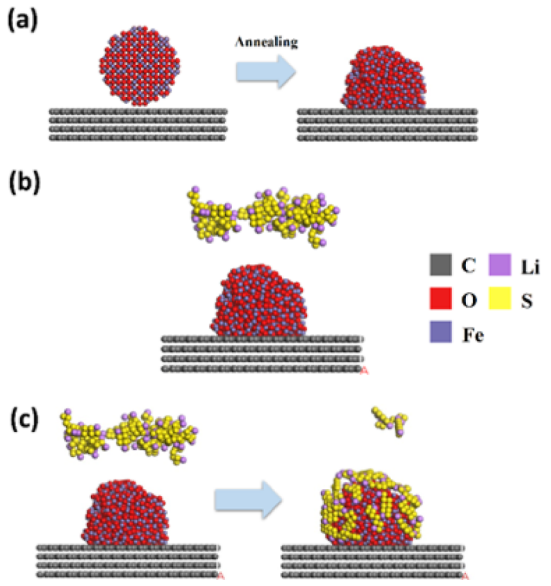


**Figure 1.** (a) The annealing progress of $Fe_3O_4$ particle supported on graphene, (b) the annealing progress of $Fe_3O_4$ particle supported on graphene, and (c) the adsorption of $Li_2S_8$ on supported $Fe_3O_4$ particle.

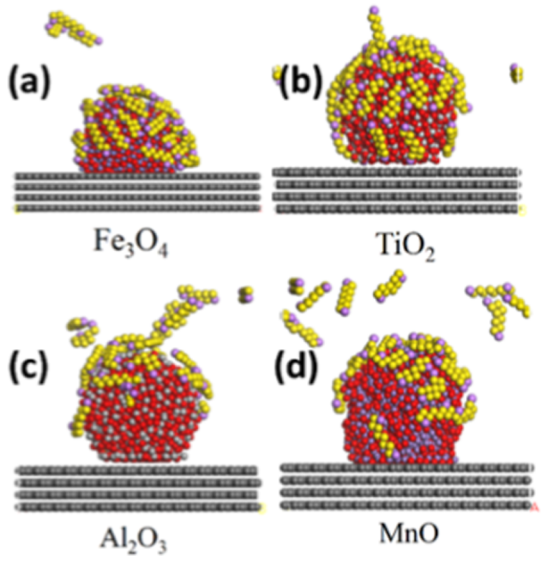


**Figure 2.** Adsorption of $Li_2S_8$ on supported (a) $Fe_3O_4$, (b) $TiO_2$, (c) $Al_2O_3$, and (d) MnO particles.

**Table 1. Adsorption Efficiency of Various Metal Oxides for $Li_2S_8$ Species in Molecular Dynamics Simulation**

| species | initial number of $Li_2S_8$ species | the number of adsorbed $Li_2S_8$ species |
|---|---|---|
| $Fe_3O_4$ | 30 | 27 |
| $TiO_2$ | 30 | 29 |
| MnO | 30 | 22 |
| $Al_2O_3$ | 30 | 17 |

molecules, indicating its superior LiPS adsorption affinity. This finding aligns with expectations and corroborates numerous reports in the literature. $Fe_3O_4$ adsorbed 27 $Li_2S_8$ molecules, making it the second most effective material, followed by $MnO_2$ and $Al_2O_3$, which adsorbed 22 and 17 molecules, respectively. Despite the high performance of titanium-based compounds, they are challenging to work with due to their low solubility in water and the need for hazardous organic solvents to achieve the solution form. Consequently, $Fe_3O_4$ was selected for this project due to its lower cost and compatibility with aqueous solutions, facilitating further reactions.

*Structure, Composition, and Chemical Interaction.* The XRD patterns of $Fe_3O_4$@Fe-AC, as depicted in Figure 3a, distinctly show the characteristic peaks of metallic Fe with reference to PDF #06−0696 in ICDD database, which are (110) peak at 44.7°, (200) peak at 65.0°, and (211) peak at 82.3°, confirming that the majority of the metal particles on the activated carbon surface are metallic metal in the activated carbon. The BET analysis reveals a surface area of 900 $m^2/g$, a total pore volume of 0.54 $cm^3/g$, and an average pore diameter of 2.4 nm. Figure 3b−d presents the results of the BET analysis, displaying the adsorption isotherm, BJH plot, and MP plot, respectively. A typical Type IV isotherm is evident in Figure 3b, highlighting the microporosity of $Fe_3O_4$@Fe-AC. The BJH plot in Figure 3c reveals a pronounced value in the $d_p$ region between 1 and 2 nm, further attesting to the microporosity of $Fe_3O_4$@Fe-AC. Meanwhile, the MP plot (Figure 3d) exhibits a broad peak ranging from dp 0.4 to 1.3 nm, suggesting that $Fe_3O_4$@Fe-AC possesses a significant number of micropores.

Figure 4 presents electron images of $Fe_3O_4$@Fe-AC. The SEM images depict that $Fe_3O_4$@Fe-AC consists of particles characterized by an irregular morphology and prominent conchoidal cavities (as illustrated in Figure 4a).[38] These cavities are advantageous for polysulfide adsorption, offering ample space to accommodate the adsorbed LiPS. The elemental mapping distinctly demonstrates the successful incorporation of Fe into the activated carbon (Figure 4b,d). The oxygen signal is detected, as shown in Figure 4c, which corresponds to the $Fe_3O_4$ outer shell. The presence of $Fe_3O_4$ is confirmed by the XPS results discussed in a later section. The TEM images, displayed in Figure 4e,f, highlight several lattice regions, ranging from 2 to 8 nm in length, dispersed on the carbon surface. The measured lattice spacing is approximately 2.91 Å, which corresponds to the crystalline microdomains of partially graphitized carbon. This structure is typically formed during the pyrolysis of carbon-rich precursors in the presence of metals, such as metallic Fe.[21,39] The presence of partially graphitized carbon regions serves as indirect evidence of the existence of metallic Fe in the $Fe_3O_4$@Fe-AC composite. Also, the 2.91 Å lattice spacing could also be the lattice of $Fe_3O_4$ as it also matches with the (220) crystalline planes of $Fe_3O_4$.[40] The morphology and elemental distribution of $Fe_3O_4$@Fe-AC were further examined by using high-resolution transmission electron microscopy (HRTEM) and energy-dispersive X-ray (EDX) mapping, as shown in Figure 5. Microsized particle with about 2 $\mu$m was observed to be embedded within the carbon matrix. Elemental mapping confirmed that these particles were rich in iron (Fe), while a weak oxygen (O) signal was also detected on the surface. This suggests that the metal particles primarily consist of metallic Fe with partial surface oxidation, consistent with the expected structure.

The chemical composition and surface functional group of $Fe_3O_4$@Fe-AC were analyzed by XPS. Figure 6a displays the full XPS spectra of $Fe_3O_4$@Fe-AC, showing that the $Fe_3O_4$@Fe-AC is composite of carbon, oxygen, and iron. The pronounced peak for oxygen, coupled with the subdued peak for Fe, suggests that $Fe_3O_4$@Fe-AC predominantly consists of carbon with Fe oxides present. In the Fe 2p spectrum (see


https://doi.org/10.1021/acs.jpcc.5c02606
J. Phys. Chem. C 2025, 129, 15507−15517

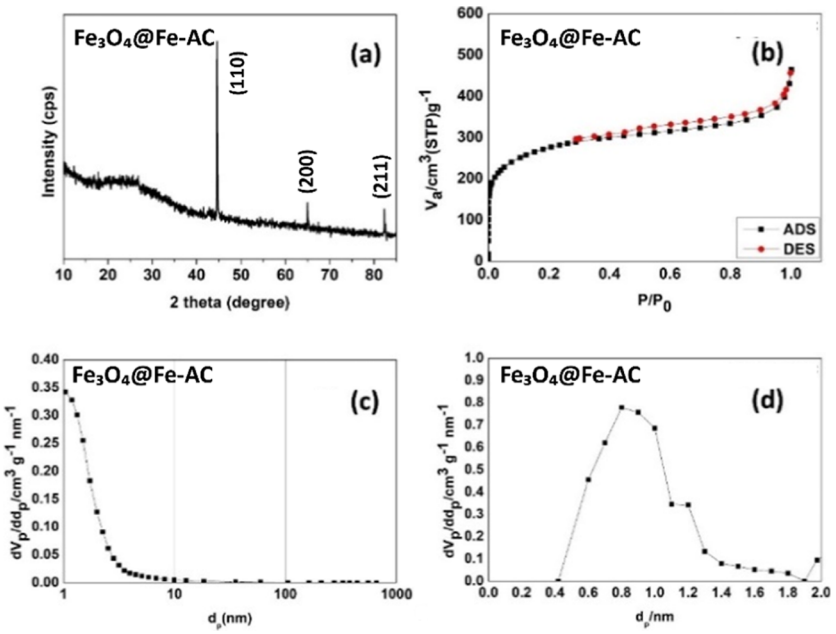


**Figure 3.** (a) XRD pattern, (b) adsorption−desorption isotherm, (c) BJH plot, and (d) MP plot of $Fe_3O_4$@Fe-AC.

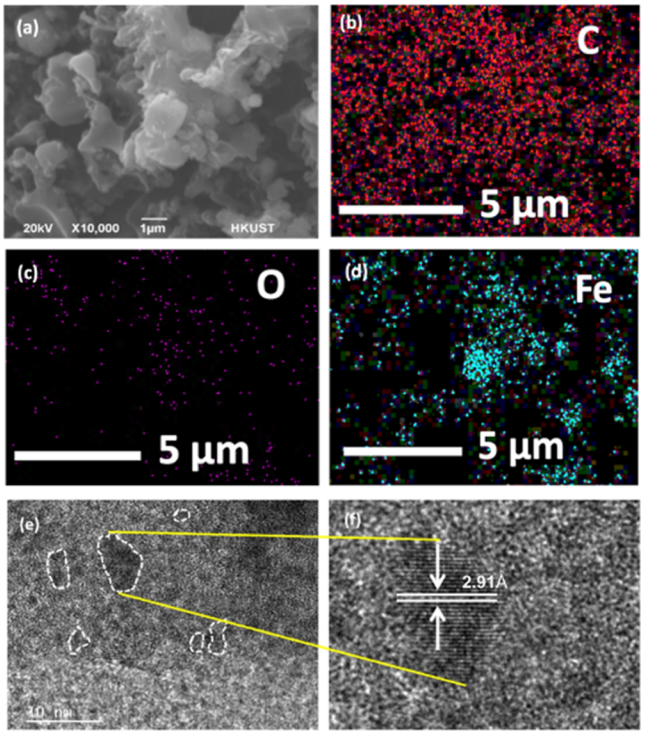


**Figure 4.** (a) SEM images of $Fe_3O_4$@Fe-AC. (b−e) Corresponding elemental mapping. (f−g) TEM images of $Fe_3O_4$@Fe-AC.

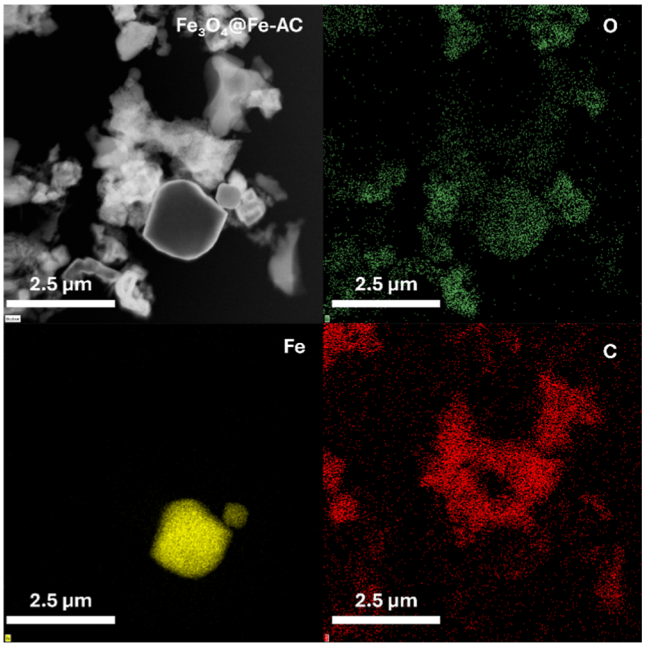


**Figure 5.** High-resolution TEM image and EDX elemental mappings of $Fe_3O_4$@Fe-AC.

Figure 6b), two distinct peaks are evident at 711 and 725 eV, which correspond to the Fe $2p_{3/2}$ and Fe $2p_{1/2}$ peaks of $Fe_3O_4$, respectively.[41,42] The O 1s spectrum features a single peak at 531.8 eV, aligning with the Fe−O bond. The XPS spectra indicate that the Fe distributed on the carbon surface exists as $Fe_3O_4$,[38] corroborating the findings from TEM images. The presence of oxides on the surface of $Fe_3O_4$@Fe-AC is reasonable as the pyrolysis conditions involving strong alkali KOH, along with $Fe^{2+}$ and $Fe^{3+}$ compounds, promoting the formation of $Fe_3O_4$. During the pyrolysis process, $Fe_3O_4$ present at the carbon−$Fe_3O_4$ interface as well as within the inner core is likely reduced by carbon, resulting in the formation of metallic iron.

As X-ray photoelectron spectroscopy (XPS) is a surface-sensitive analytical technique that detects the chemical composition within a depth of approximately 1−10 nm, while X-ray diffraction (XRD) provides information from the bulk of the material, the difference in analytical depth accounts for the observed discrepancy between the two results. XRD analysis indicates that the overall Fe phase in the carbon is metallic, whereas XPS reveals that the surface of the Fe particles exists in the form of $Fe_3O_4$. This inconsistency suggests that the outer surface of the activated carbon is



https://doi.org/10.1021/acs.jpcc.5c02606
J. Phys. Chem. C 2025, 129, 15507−15517

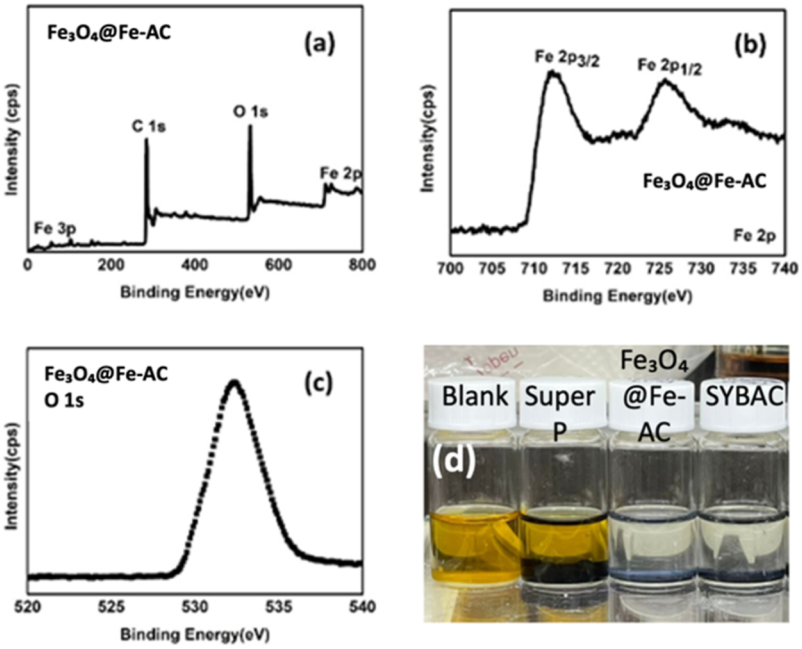


**Figure 6.** (a) Full XPS spectrum, (b) Fe 2p spectrum, and (c) O 1s spectrum of $Fe_3O_4$@Fe-AC, and (d) visible adsorption test.

covered by $Fe_3O_4$, while the inner core, which constitutes the majority of the activated carbon particles, remains in the reduced metallic Fe state. These findings provide clear evidence supporting the core−shell structure of $Fe_3O_4$@Fe activated carbon. An illustration of $Fe_3O_4$ @Fe-AC is shown in Figure 7.

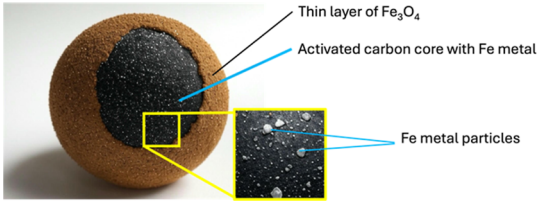


**Figure 7.** Illustration of $Fe_3O_4$@Fe-AC.

To assess the polysulfide adsorption capability of $Fe_3O_4$@Fe-AC, an adsorption test was performed in an argon-filled glovebox. $Fe_3O_4$@Fe-AC, Super P carbon, and SYBAC were introduced into the LiPS solution for adsorption and the color change of the solution. The pronounced affinity of $Fe_3O_4$@Fe-AC and SYBAC for LiPS is evident in Figure 6d. The originally orange-colored LiPS solution became decolorized within 20 min when in contact with $Fe_3O_4$@Fe-AC and SYBAC. In contrast, the solution with Super P carbon exhibited only minor color changes. It matches with the previous report that activated carbon can provide physical adsorption to LiPS because of the high-surface area.[38] This experiment unequivocally demonstrates the superior LiPS adsorption ability of the activated carbon compared with Super P carbon.

To further investigate the adsorption of LiPS by the $Fe_3O_4$@Fe-AC composite, DFT simulations were performed to examine the interaction between $Li_2S_4$ molecules and $Fe_3O_4$. The total energy of the system was calculated before and after adsorption to determine the energetic changes associated with the process, as illustrated in the schematic diagram in Figure 8. The results indicate that the adsorption process is exothermic

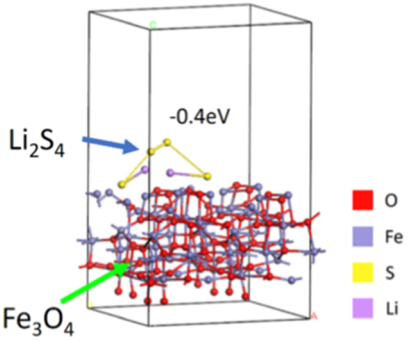


**Figure 8.** Schematic diagram of the adsorption of LiPS of $Fe_3O_4$.

with an energy release of 0.4 eV following adsorption. This energy release suggests that the system attains a more stable state upon adsorption, implying a strong interaction between $Li_2S_4$ molecules and the $Fe_3O_4$ composite.

*Electrochemical Performance.* To assess the electrochemical performance of $Fe_3O_4$@Fe-AC as a cathode material in Li−S batteries, CR2016 coin-type cells were assembled with metallic lithium serving as the counter electrode.Figure 9a depicts the cyclic performance of $Fe_3O_4$@Fe-AC/S batteries, each containing a sulfur loading ranging from 0.9 to 1.1 mg, tested at current densities of 0.5C, 2C, and 3C.

At a current density of 0.5C, the battery exhibited an initial discharge capacity of 755 mAh/g (recorded during the 11th cycle) and maintained a discharge capacity of 572 mAh/g by the 500th cycle, corresponding to an overall decay rate of 0.050% per cycle. When operated at 2C, the initial discharge capacity was 751 mAh/g (11th cycle), which decreased to 510 mAh/g by the 500th cycle, reflecting an overall decay rate of 0.066% per cycle. At a higher current density of 3C, the initial discharge capacity stood at 557 mAh/g (11th cycle) and diminished to 367 mAh/g by the 500th cycle, with an overall decay rate of 0.070% per cycle. Based on the results of this test, although the decay rate shows a slight increase with the rise in


https://doi.org/10.1021/acs.jpcc.5c02606
J. Phys. Chem. C 2025, 129, 15507−15517

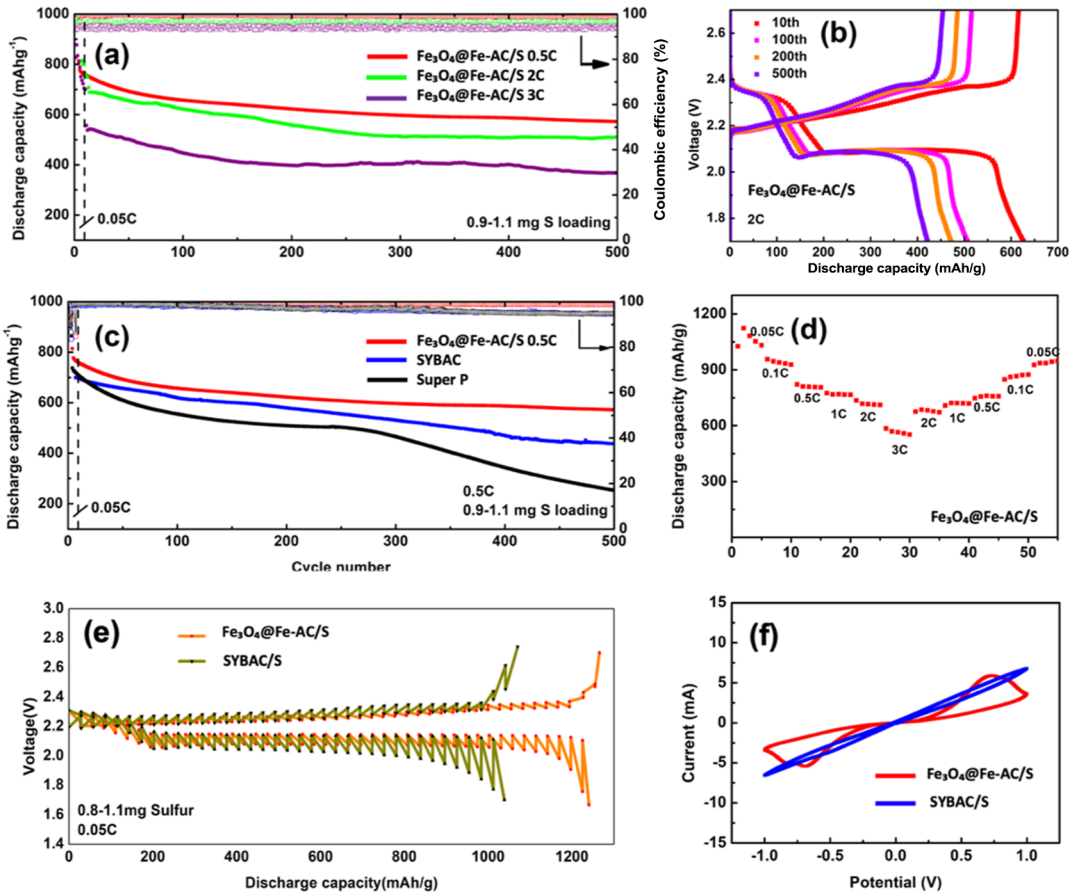


**Figure 9.** (a) Cycling performances of the $Fe_3O_4$@Fe-AC/S cathode at different rates, (b) galvanostatic charge and discharge profiles of the $Fe_3O_4$@Fe-AC/S cathode at 2C, (c) cycling performances of the $Fe_3O_4$@Fe-AC/S cathode, SYBAC/S cathode, and Super P/S cathode, (d) rate performance at different current densities with the $Fe_3O_4$@Fe-AC/S cathode, (e) GITT performance of the $Fe_3O_4$@Fe-AC/S battery and SYBAC/S battery, and (f) CV profile of $Fe_3O_4$@Fe-AC/S and SYBAC/S symmetrical cells.

C-rate, it remains at a low level, indicating that $Fe_3O_4$@Fe-AC is highly effective in controlling LiPS.

Figure 9b presents the galvanostatic charge and discharge profiles of the $Fe_3O_4$@Fe-AC/S cathode at 2C. Two distinct plateaus in the discharge curves indicate a two-step reaction occurring in the sulfur cathode. The first plateau at 2.36 V corresponds to the redox reaction that converts sulfur into long-chain lithium LiPS. The subsequent plateau at 2.10 V signifies the transformation of these long-chain LiPS into short-chain variants.[14] These profiles are critical for analyzing the polarization potential, defined as the voltage difference between the charge and discharge curves. A lower polarization potential indicates reduced internal resistance and improved reaction kinetics, while a higher potential suggests the opposite.

The $Fe_3O_4$@Fe-AC/S cathode consistently exhibits polarization potentials of 0.196, 0.193, 0.191, and 0.195 V during the 100th, 200th, and 500th cycles at 0.5C, respectively. This stability underscores $Fe_3O_4$@Fe-AC's ability to maintain consistent reaction kinetics, further emphasizing its superior LiPS adsorption capability. In contrast, the Super P/S battery registered significantly higher polarization potentials of 0.377, 0.415, and 0.395 V (Figure S1), highlighting the enhanced performance of $Fe_3O_4$@Fe-AC.

Figure 9c compares the cyclic performance of the $Fe_3O_4$@Fe-AC/S battery, Super P/S battery, and SYBAC/S battery. The $Fe_3O_4$@Fe-AC/S battery demonstrates superior performance compared to both the Super P/S and SYBAC/S batteries when analyzing the discharge capacity at the 11th cycle and the overall decay rate up to the 500th cycle. At the 11th cycle, the $Fe_3O_4$@Fe-AC/S battery exhibits a robust discharge capacity of approximately 755 mAh/g, whereas the Super P/S and SYBAC/S batteries display slightly lower capacities of 694 mAh/g and significantly lower capacities at 703 mAh/g, respectively. This initial performance advantage is further underscored by the decay rate observed over the cycling period. The $Fe_3O_4$@Fe-AC/S battery shows a minimal decay rate of 0.050% per cycle, which is notably lower than the 0.076% per cycle observed for Super P/S and the 0.13% per cycle for SYBAC/S, indicating that the $Fe_3O_4$@Fe-AC/S battery retains a higher degree of stability and maintains its capacity more effectively over time.

When the plotted discharge capacities are examined, it becomes evident that the SYBAC/S battery suffers a sharp decline in capacity after approximately 250 cycles, reflecting a significant loss in performance. In stark contrast, the $Fe_3O_4$@Fe-AC/S battery maintains a steady discharge capacity throughout the 500 cycles, without experiencing such a dramatic drop. This stability highlights the effective role of $Fe_3O_4$ nanoparticles in controlling the LiPS shuttle effect, thus contributing to the enhanced overall performance and durability of the battery.

Figure 9d illustrates the rate capability of $Fe_3O_4$@Fe-AC/S batteries across various current densities. The battery



https://doi.org/10.1021/acs.jpcc.5c02606
J. Phys. Chem. C 2025, 129, 15507−15517

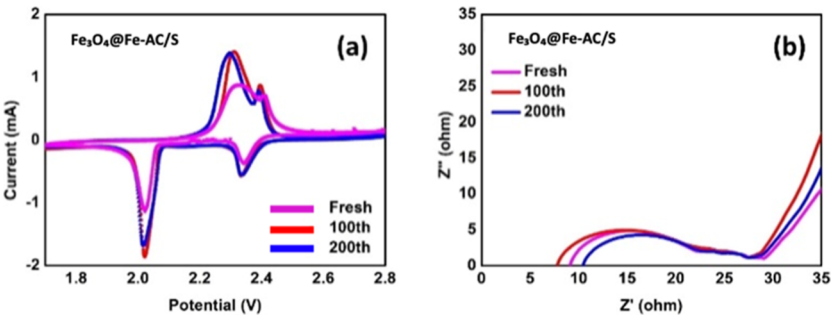


**Figure 10.** (a) CV and (b) EIS curves (Nyquist plot) of the $Fe_3O_4$@Fe-AC/S battery.

**Table 2. Comparative Performance of Various Cathode Materials for Lithium−Sulfur Batteries from Literature**

| material | initial capacity | C-rate | decay rate (%/cycle) | cycle number | year of publication | ref |
|---|---|---|---|---|---|---|
| $Fe_3O_4$@Fe-AC | 751 | 2 | 0.066 | 500 | this work | this work |
| $A_5$HNT@NC/S | 691.2 | 0.5 | 0.107 | 150 | 2025 | 47 |
| $Fe_2O_3/SnO_2$ QDs@S | 750 | 0.2 | 0.4 | 100 | 2024 | 45 |
| $Co/CoV_2O_6$ | 558.40 | 0.2 | 0.29 | 100 | 2024 | 48 |
| S/CoO-CoP-CNT | 979 | 0.2 | 0.31 | 200 | 2023 | 49 |
| $Fe_3O_4/Fe_xS_y$ heterostructures | 683 | 0.5 | 0.067 | 500 | 2022 | 50 |
| $Fe_2P$-NPC | 800 | 0.1 | 0.24 | 200 | 2022 | 51 |
| 1D-$Fe_3O_4$@C/S | 791 | 0.5 | 0.115 | 200 | 2021 | 52 |
| $Fe_3C$/PB@S | 837.6 | 1 | 0.135 | 250 | 2021 | 53 |
| $Fe_3O_4$-seated rGO−sulfur complex | 573 | 0.5 | no info | no info | 2020 | 54 |
| CNT/$Fe_3O_4$ | 753 | 1 | 0.084 | 300 | 2019 | 46 |

demonstrates impressive capacities of 1123 mAh/g at 0.05C, 957 mAh/g at 0.1C, 821 mAh/g at 0.5C, 775 mAh/g at 1C, 736 mAh/g at 2C, and 585 mAh/g at 3C. Notably, when the current density is reverted to its initial value in subsequent cycles, the battery retains its rate capabilities remarkably well, achieving retention rates of 83.5%, 90.1%, 92.1%, 91.2%, and 93.1% at 0.05C, 0.1C, 0.5C, 1C, and 2C, respectively. These results underscore the battery's stability and exceptional rate performance, indicating its ability to sustain high capacities even under varying current loads. The galvanostatic intermittent titration test (GITT) studies of $Fe_3O_4$@Fe-AC and SYBAC/S with similar sulfur loadings, as shown in Figure 9e, elucidate the kinetic and thermodynamic advantages of $Fe_3O_4$@Fe-AC over SYBAC. Both GITT profiles exhibit characteristic discharge−charge curves typical of Li−S batteries. However, the $Fe_3O_4$@Fe-AC/S electrode demonstrates more stable and higher plateau capacities with minimal polarization, indicating a superior reaction kinetics. Furthermore, the deviation between the practical voltages during constant current pulses and the equilibrium voltages at steady state, as a function of the state of discharge and charge, reflects the chemical diffusion coefficient of the electrode during the relaxation process. The voltage of the $Fe_3O_4$@Fe-AC/S electrode generally relaxes more rapidly to equilibrium, with significantly smaller voltage deviations, particularly during the discharge process.[25] This behavior suggests a high diffusion coefficient and strong binding of LiPS to the $Fe_3O_4$@Fe-AC electrode.

To evaluate the electrochemical stability and electrocatalytic activity of different catalysts toward polysulfide conversion, CV tests were conducted in symmetric batteries at a scan rate of 10 mV $s^{-1}$. The CV profiles are listed in Figure 9f. The $Fe_3O_4$@Fe-AC electrode exhibits a distinct reduction peak at − 0.71 V, corresponding to the reduction of short-chain lithium polysulfides (LiPS) to $Li_2S_2/Li_2S$. Additionally, a well-defined oxidation peak at 0.71 V is associated with the oxidation of short-chain LiPS to long-chain LiPS.[43] In contrast, the CV curve of the SYBAC/S battery does not display any observable peaks, indicating an absence of catalytic activity toward LiPS conversion. This comparison suggests that the catalytic performance for LiPS conversion primarily originates from the $Fe_3O_4$@Fe particles on the activated carbon surface.

The electrochemical reversibility and chemical kinetics of the $Fe_3O_4$@Fe-AC/S battery were investigated by using cyclic voltammetry (CV), with the resulting curves presented in Figure 10a. Each curve displays the characteristic four redox peaks typical of lithium−sulfur batteries, consisting of two reduction peaks and two oxidation peaks. During the cathodic scan, peaks centered at approximately 2.3 V indicate the reduction of elemental sulfur to high-order LiPS, while those around 2.0 V correspond to the further reduction from high-order to low-order LiPS, ultimately leading to the formation of $Li_2S_2/Li_2S$.[44] In contrast, during the anodic scan, oxidation peaks near 2.3 V represent the reconversion of low-order LiPS back to high-order LiPS, while peaks close to 2.45 V denote the oxidation of high-order LiPS to elemental sulfur.

The morphology of the peaks from a newly assembled battery appears broader and less pronounced, which could be due to an initial sulfur imbalance that restricts ion transfer and prevents some sulfur from participating in the reaction. However, after 100 cycles, the peaks become sharper and more defined, indicating improved reaction kinetics. When comparing the curves from the 100th and 200th cycles, the two are largely congruent with only a slight reduction in peak height, while the peak positions remain consistent. This behavior underscores the high reversibility and cycling stability of the $Fe_3O_4$@Fe-AC/S battery.

Electrochemical impedance spectroscopy (EIS) tests provide further insights into the reaction kinetics of the $Fe_3O_4$@Fe-AC/S battery, which is shown inFigure 10b. Typically, a


https://doi.org/10.1021/acs.jpcc.5c02606
J. Phys. Chem. C 2025, 129, 15507−15517

Nyquist plot features a depressed semicircle in the high-frequency region and a sloping line in the low-frequency region. The semicircle represents the charge transfer resistance ($R_{CT}$) between the electrode and the electrolyte, while the sloping line is associated with Warburg impedance ($Z_W$), which signifies diffusion processes within the electrode material. The curve's starting point, denoted as $R_s$, represents the series resistance, encompassing the ionic resistance of the electrolyte, the resistance of the current collector, and the intrinsic resistance of the electrode materials.[9] The $Fe_3O_4$@Fe-AC/S battery exhibits three similar Nyquist plots for the freshly assembled battery and after 100 and 200 cycles, respectively, indicating stable reaction kinetics. Specifically, the $R_{CT}$ for the fresh battery is 13.2 Ω, which slightly increases to 14.8 Ω after 100 cycles and then decreases to 12.2 Ω after 200 cycles. The relative stability of $R_{CT}$ suggests that the $Fe_3O_4$@Fe-AC material effectively maintains the battery's state of health, likely due to its effective control over polysulfide diffusion, contributing to the overall stability and longevity of the battery's electrochemical performance (Figure 10).

As shown in Table 2, $Fe_3O_4$@Fe-AC exhibits several distinct advantages over similar materials reported in the literature. The $Fe_3O_4$@Fe-AC/S battery delivers an initial discharge capacity of 751 mAh/g at 2C, with a minimal capacity decay rate of only 0.066% per cycle. Notably, the initial discharge capacity is significantly higher and the capacity decay rate is substantially lower than those of most materials presented in Table 2, even though those materials were tested under lower C-rate conditions. For instance, $Fe_2O_3/SnO_2$ QDs@S achieves a capacity of only 750 mAh/g at 0.2C, with a considerably higher decay rate of 0.4% per cycle over 100 cycles.[45] Similarly, CNT/$Fe_3O_4$ delivers a capacity of 753 mAh/g at 0.5C but exhibits a higher decay rate of 0.084% per cycle.[46] Beyond its superior electrochemical performance, $Fe_3O_4$@Fe-AC is the only cathode material synthesized from waste resources, utilizing a simple and sustainable fabrication process consisting of a single pyrolysis step. This approach not only enables the valorization of waste materials but also promotes the environmentally friendly battery technology.

## CONCLUSIONS

This study presents $Fe_3O_4$@Fe-AC as an effective sulfur host for Li−S batteries, offering a dual-functional mechanism that significantly suppresses the polysulfide shuttle effect while enhancing the reaction kinetics. The combination of high-surface-area activated carbon, $Fe_3O_4$ for strong LiPS adsorption, and Fe for catalytic conversion results in exceptional cyclic stability, as demonstrated by an ultralow decay rate of 0.050% per cycle over 500 cycles at 0.5C and a high rate capability of 557 mAh/g initially at 3C, maintaining 367 mAh/g after 500 cycles. The material also exhibits a stable charge transfer resistance and a low polarization potential, ensuring long-term electrochemical stability. Additionally, $Fe_3O_4$@Fe-AC is synthesized through a cost-effective and sustainable approach using soybean waste (okara) as a carbon precursor, aligning with green energy initiatives. Its intrinsic magnetism enables potential recyclability, further enhancing its environmental benefits. With its scalable synthesis, high-performance electrochemical properties, and sustainability advantages, $Fe_3O_4$@Fe-AC represents a promising step toward commercial Li−S batteries with enhanced stability and environmental responsibility.

## ASSOCIATED CONTENT

### Supporting Information

The Supporting Information is available free of charge at https://pubs.acs.org/doi/10.1021/acs.jpcc.5c02606.

Force field parameters, details of molecular dynamics simulations, and additional galvanostatic charge/discharge profiles (PDF)

## AUTHOR INFORMATION


### Corresponding Authors

**Leung Yuk Frank Lam** − *Department of Chemical and Biological Engineering, The Hong Kong University of Science and Technology, Kowloon 999077 Hong Kong S.A.R., China*; Email: kefrank@ust.hk

**Xijun Hu** − *Department of Chemical and Biological Engineering, The Hong Kong University of Science and Technology, Kowloon 999077 Hong Kong S.A.R., China*; orcid.org/0000-0001-5561-5246; Email: kexhu@ust.hk

### Authors

**Ka Chun Li** − *Department of Chemical and Biological Engineering, The Hong Kong University of Science and Technology, Kowloon 999077 Hong Kong S.A.R., China*; orcid.org/0000-0001-9370-3554

**Feng Shi** − *Department of Chemical Engineering, Zhejiang University of Technology, Hangzhou 310014, China*

**Xuanming Chen** − *Department of Chemical and Biological Engineering, The Hong Kong University of Science and Technology, Kowloon 999077 Hong Kong S.A.R., China*

**Zeyuan Di** − *Department of Chemical and Biological Engineering, The Hong Kong University of Science and Technology, Kowloon 999077 Hong Kong S.A.R., China*; orcid.org/0009-0000-9611-5176

**Moyu Hu** − *Department of Chemical and Biological Engineering, The Hong Kong University of Science and Technology, Kowloon 999077 Hong Kong S.A.R., China*; orcid.org/0000-0002-6018-7677

**Long Bun Sin** − *Department of Chemical and Biological Engineering, The Hong Kong University of Science and Technology, Kowloon 999077 Hong Kong S.A.R., China*; orcid.org/0009-0001-6398-7573

**Chi Ho Wong** − *Division of Science, Engineering and Health Studies, School of Professional Education and Executive Development, The Hong Kong Polytechnic University, Kowloon 999077 Hong Kong S.A.R., China*

Complete contact information is available at: https://pubs.acs.org/10.1021/acs.jpcc.5c02606


### Author Contributions

K.C.L. and F.S. contributed equally. Ka Chun Li: investigation, performing the experiment, data collection, writing, and revising the manuscript; Feng Shi: MD calculation and manuscript revising; Zeyuan Di: manuscript revising; Xuanming Chen: DFT calculation; Moyu Hu: manuscript revising; Long Bun Sin: manuscript revising; Chi Ho Wong: DFT calculation and manuscript revising; Xijun Hu: supervision and manuscript revising; and Leung Yuk Frank Lam: supervision and manuscript revising.

### Notes

The authors declare no competing financial interest.



https://doi.org/10.1021/acs.jpcc.5c02606
J. Phys. Chem. C 2025, 129, 15507−15517

## ■ ACKNOWLEDGMENTS

We gratefully acknowledge the financial support for this research from Vitasoy International Holding Ltd. We also appreciate the technical assistance from Materials Characterization & Preparation Facility (MCPF) at HKUST.

## ■ REFERENCES

(1) Peng, H. J.; Huang, J. Q.; Zhao, M. Q.; Zhang, Q.; Cheng, X. B.; Liu, X. Y.; Qian, W. Z.; Wei, F. Nanoarchitectured Graphene/CNT@porous Carbon with Extraordinary Electrical Conductivity and Interconnected Micro/Mesopores for Lithium-Sulfur Batteries. *Adv. Funct. Mater.* **2014**, *24* (19), 2772−2781.

(2) Sun, H.; Xu, G. L.; Xu, Y. F.; Sun, S. G.; Zhang, X.; Qiu, Y.; Yang, S. A Composite Material of Uniformly Dispersed Sulfur on Reduced Graphene Oxide: Aqueous One-Pot Synthesis, Characterization and Excellent Performance as the Cathode in Rechargeable Lithium-Sulfur Batteries. *Nano Res.* **2012**, *5* (10), 726−738.

(3) Mi, K.; Jiang, Y.; Feng, J.; Qian, Y.; Xiong, S. Hierarchical Carbon Nanotubes with a Thick Microporous Wall and Inner Channel as Efficient Scaffolds for Lithium-Sulfur Batteries. *Adv. Funct. Mater.* **2016**, *26* (10), 1571−1579.

(4) Sultanov, F.; Zhumasheva, N.; Dangaliyeva, A.; Zhaisanova, A.; Baikalov, N.; Tatykayev, B.; Yeleuov, M.; Bakenov, Z.; Mentbayeva, A. Enhancing Lithium-Sulfur Battery Performance with Biomass-Derived Graphene-like Porous Carbon and NiO Nanoparticles Composites. *J. Power Sources* **2024**, *593*, 233959.

(5) Liu, W.; Fan, X.; Xu, B.; Chen, P.; Tang, D.; Meng, F.; Zhou, R.; Liu, J.; Fancheng Meng, C. MnO-Inlaid Hierarchically Porous Carbon Hybrid for Lithium-Sulfur Batteries. *Nano Select* **2021**, *2* (3), 573−580.

(6) Yu, M.; Yuan, W.; Li, C.; Hong, J. D.; Shi, G. Performance Enhancement of a Graphene-Sulfur Composite as a Lithium-Sulfur Battery Electrode by Coating with an Ultrathin Al2O3 Film via Atomic Layer Deposition. *J. Mater. Chem. A* **2014**, *2* (20), 7360−7366.

(7) Zheng, C.; Niu, S.; Lv, W.; Zhou, G.; Li, J.; Fan, S.; Deng, Y.; Pan, Z.; Li, B.; Kang, F.; et al. Propelling Polysulfides Transformation for High-Rate and Long-Life Lithium−Sulfur Batteries. *Nano Energy* **2017**, *33*, 306−312.

(8) Wei Seh, Z.; Li, W.; Cha, J. J.; Zheng, G.; Yang, Y.; McDowell, M. T.; Hsu, P.-C.; Cui, Y. Sulphur−TiO2 Yolk−Shell Nanoarchitecture with Internal Void Space for Long-Cycle Lithium−Sulphur Batteries. *Nat. Commun.* **2013**, *4* (1), 1331.

(9) Sabbaghi, A.; Wong, C. H.; Hu, X.; Lam, F. L. Y. Titanium Dioxide Nanotube Arrays (TNTAs) as an Effective Electrocatalyst Interlayer for Sustainable High-Energy Density Lithium-Sulfur Batteries. *J. Alloys Compd.* **2022**, *899*, 163268.

(10) Yao, W.; Chu, C.; Zheng, W.; Zhan, L.; Wang, Y. "Pea-Pod-like" Nitrogen-Doped Hollow Porous Carbon Cathode Hosts Decorated with Polar Titanium Dioxide Nanocrystals as Efficient Polysulfide Reservoirs for Advanced Lithium−Sulfur Batteries. *J. Mater. Chem. A* **2018**, *6*, 18191−18205.

(11) Abedi, S.; Karimi, B.; Kazemi, F.; Bostina, M.; Vali, H. Amorphous TiO2 Coated into Periodic Mesoporous Organosilicate Channels as a New Binary Photocatalyst for Regeneration of Carbonyl Compounds from Oximes under Sunlight Irradiation. *Org. Biomol. Chem.* **2013**, *11* (3), 416−419.

(12) Salhabi, E. H. M.; Zhao, J.; Wang, J.; Yang, M.; Wang, B.; Wang, D. Hollow Multi-Shelled Structural TiO2−x with Multiple Spatial Confinement for Long-Life Lithium−Sulfur Batteries. *Angew. Chem., Int. Ed.* **2019**, *58* (27), 9078−9082.

(13) Zhou, T.; Lv, W.; Li, J.; Zhou, G.; Zhao, Y.; Fan, S.; Liu, B.; Li, B.; Kang, F.; Yang, Q. H. Twinborn TiO2−TiN Heterostructures Enabling Smooth Trapping−Diffusion−Conversion of Polysulfides towards Ultralong Life Lithium−Sulfur Batteries. *Energy Environ. Sci.* **2017**, *10* (7), 1694−1703.

(14) Cui, Z.; Yao, J.; Mei, T.; Zhou, S.; Hou, B.; Li, J.; Li, J.; Wang, J.; Qian, J.; Wang, X. Strong Lithium Polysulfides Chemical Trapping of TiC-TiO2/S Composite for Long-Cycle Lithium-Sulfur Batteries. *Electrochim. Acta* **2019**, *298*, 43−51.

(15) Xiao, Z.; Yang, Z.; Wang, L.; Nie, H.; Zhong, M.; Lai, Q.; Xu, X.; Zhang, L.; Huang, S. A Lightweight TiO2/Graphene Interlayer, Applied as a Highly Effective Polysulfide Absorbent for Fast, Long-Life Lithium-Sulfur Batteries. *Adv. Mater.* **2015**, *27* (18), 2891−2898.

(16) Liu, S.; Li, Y.; Zhang, C.; Chen, X.; Wang, Z.; Cui, F.; Yang, X.; Yue, W. Amorphous TiO2 Nanofilm Interface Coating on Mesoporous Carbon as Efficient Sulfur Host for Lithium−Sulfur Batteries. *Electrochim. Acta* **2020**, *332*, 135458.

(17) Qi, C.; Cai, M.; Li, Z.; Jin, J.; Chowdari, B. V. R.; Chen, C.; Wen, Z. Ultrathin TiO2 Surface Layer Coated TiN Nanoparticles in Freestanding Film for High Sulfur Loading Li-S Battery. *Chem. Eng. J.* **2020**, *399*, 125674.

(18) Adi, A.; Taniguchi, I. Synthesis of an Advanced Sulfur Cathode with a Porous Graphitic C/Fe3C Electrocatalyst and Three-Dimensional Current Collector for Li-S Batteries. *Energy Fuels* **2023**, *37* (18), 14324−14333.

(19) Xiong, Z.; Li, J.; Sun, Y.; Lin, Y.; Du, L.; Wei, Z.; Wu, M.; Shi, K.; Liu, Q. Fe3C@NCNT as a Promoter for the Sulfur Cathode toward High-Performance Lithium-Sulfur Batteries. *J. Alloys Compd.* **2022**, *899*, 163245.

(20) Wang, C.; Song, H.; Yu, C.; Ullah, Z.; Guan, Z.; Chu, R.; Zhang, Y.; Zhao, L.; Li, Q.; Liu, L. Iron Single-Atom Catalyst Anchored on Nitrogen-Rich MOF-Derived Carbon Nanocage to Accelerate Polysulfide Redox Conversion for Lithium Sulfur Batteries. *J. Mater. Chem. A* **2020**, *8* (6), 3421−3430.

(21) Liu, Z.; Zhou, L.; Ge, Q.; Chen, R.; Ni, M.; Utetiwabo, W.; Zhang, X.; Yang, W. Atomic Iron Catalysis of Polysulfide Conversion in Lithium-Sulfur Batteries. *ACS Appl. Mater. Interfaces* **2018**, *10* (23), 19311−19317.

(22) Sun, Q.; He, B.; Zhang, X. Q.; Lu, A. H. Engineering of Hollow Core-Shell Interlinked Carbon Spheres for Highly Stable Lithium-Sulfur Batteries. *ACS Nano* **2015**, *9* (8), 8504−8513.

(23) Chen, W.; Qian, T.; Xiong, J.; Xu, N.; Liu, X.; Liu, J.; Zhou, J.; Shen, X.; Yang, T.; Chen, Y.; et al. A New Type of Multifunctional Polar Binder: Toward Practical Application of High-Energy Lithium−Sulfur Batteries. *Adv. Mater.* **2017**, *29* (12), 1605160.

(24) Zhang, X.; Yuan, W.; Yang, Y.; Chen, Y.; Tang, Z.; Wang, C.; Yuan, Y.; Ye, Y.; Wu, Y.; Tang, Y. Immobilizing Polysulfide by In Situ Topochemical Oxidation Derivative TiC@Carbon-Included TiO2 Core−Shell Sulfur Hosts for Advanced Lithium−Sulfur Batteries. *Small* **2020**, *16* (52), 2005998.

(25) Wang, X.; Yang, Y.; Lai, C.; Li, R.; Xu, H.; Tan, D. H. S.; Zhang, K.; Yu, W.; Fjeldberg, O.; Lin, M.; Tang, W.; Meng, Y. S.; Loh, K. P. Dense-Stacking Porous Conjugated Polymer as Reactive-Type Host for High-Performance Lithium Sulfur Batteries. *Angew. Chem., Int. Ed.* **2021**, *60* (20), 11359−11369.

(26) Plimpton, S. Fast Parallel Algorithms for Short-Range Molecular Dynamics. *J. Comput. Phys.* **1995**, *117* (1), 1−19.

(27) Byggmästar, J.; Nagel, M.; Albe, K.; Henriksson, K. O. E.; Nordlund, K. Analytical Interatomic Bond-Order Potential for Simulations of Oxygen Defects in Iron. *J. Phys.: Condens. Matter* **2019**, *31* (21), 215401.

(28) Stuart, S. J.; Tutein, A. B.; Harrison, J. A. A. Reactive Potential for Hydrocarbons with Intermolecular Interactions. *J. Chem. Phys.* **2000**, *112* (14), 6472−6486.

(29) Sun, H.; Mumby, S. J.; Maple, J. R.; Hagler, A. T. An Ab Initio CFF93 All-Atom Force Field for Polycarbonates. *J. Am. Chem. Soc.* **1994**, *116* (7), 2978−2987.

(30) Cui, W.; Yu, S.; Zhao, J. Two-Dimensional $\pi$-Conjugated Metal Bis(Dithiolene) Nanosheet: A Promising Anchoring Material for Lithium-Sulfur Batteries. *Comput. Mater. Sci.* **2020**, *171*, 109228.

(31) Ma, D.; Hu, B.; Wu, W.; Liu, X.; Zai, J.; Shu, C.; Tadesse Tsega, T.; Chen, L.; Qian, X.; Liu, T. L. Highly Active Nanostructured $CoS_2$/CoS Heterojunction Electrocatalysts for Aqueous Polysulfide/Iodide Redox Flow Batteries. *Nat. Commun.* **2019**, *10* (1), 3367.



https://doi.org/10.1021/acs.jpcc.5c02606
J. Phys. Chem. C 2025, 129, 15507−15517

(32) Pan, H. Graphitic Carbon Nitride Nanotubes As Li-Ion Battery Materials: A First-Principles Study. *J. Phys. Chem. C* **2014**, *118* (18), 9318−9323.
(33) Tang, R.; Zhang, R.; Shi, C.; Liu, E.; Zhao, N. Ni0.85Se Nanoparticles Anchored on RGO as an Efficient Polysulfides Immobilizer for Lithium-Sulfur Batteries. *Int. J. Electrochem. Sci.* **2023**, *18* (10), 100289.
(34) Li, G.; Wang, X.; Seo, M. H.; Li, M.; Ma, L.; Yuan, Y.; Wu, T.; Yu, A.; Wang, S.; Lu, J.; et al. Chemisorption of Polysulfides through Redox Reactions with Organic Molecules for Lithium−Sulfur Batteries. *Nat. Commun.* **2018**, *9*, 1−10.
(35) Zhang, Q.; Zhang, X.; Xiao, Y.; Li, C.; Tan, H. H.; Liu, J.; Wu, Y. Theoretical Insights into the Favorable Functionalized Ti2C-Based MXenes for Lithium-Sulfur Batteries. *ACS Omega* **2020**, *5* (45), 29272−29283.
(36) Fang, M.; Han, J.; He, S.; Ren, J. C.; Li, S.; Liu, W. Effective Screening Descriptor for MXenes to Enhance Sulfur Reduction in Lithium-Sulfur Batteries. *J. Am. Chem. Soc.* **2023**, *145* (23), 12601−12608.
(37) Stukowski, A.; In, S. Visualization and Analysis of Atomistic Simulation Data with OVITO−the Open Visualization Tool. *Model. Simulat. Mater. Sci. Eng.* **2009**, *18* (1), 015012.
(38) Ren, G.; Li, S.; Fan, Z. X.; Warzywoda, J.; Fan, Z. Soybean-Derived Hierarchical Porous Carbon with Large Sulfur Loading and Sulfur Content for High-Performance Lithium−Sulfur Batteries. *J. Mater. Chem. A* **2016**, *4* (42), 16507−16515.
(39) Goldie, S. J.; Coleman, K. S. Graphitization by Metal Particles. *ACS Omega* **2023**, *8* (3), 3278−3285.
(40) Wang, X.; Zhang, M.; Zhao, J.; Huang, G.; Sun, H. Fe3O4@ polyaniline Yolk-Shell Micro/Nanospheres as Bifunctional Materials for Lithium Storage and Electromagnetic Wave Absorption. *Appl. Surf. Sci.* **2018**, *427*, 1054−1063.
(41) Han, F.; Ma, L.; Sun, Q.; Lei, C.; Lu, A. Rationally Designed Carbon-Coated Fe3O4 Coaxial Nanotubes with Hierarchical Porosity as High-Rate Anodes for Lithium Ion Batteries. *Nano Res.* **2014**, *7* (11), 1706−1717.
(42) Kohzadi, H.; Soleiman-Beigi, M. XPS and Structural Studies of Fe3O4-PTMS-NAS@Cu as a Novel Magnetic Natural Asphalt Base Network and Recoverable Nanocatalyst for the Synthesis of Biaryl Compounds. *Sci. Rep.* **2021**, *11* (1), 1−14.
(43) Jiao, X.; Tang, X.; Li, J.; Xiang, Y.; Li, C.; Tong, C.; Shao, M.; Wei, Z. Toward Robust Lithium−Sulfur Batteries via Advancing Li 2 S Deposition. *Chem. Sci.* **2024**, *15* (21), 7949−7964.
(44) *Lithium−Sulfur Batteries*; Wild, M., Offer, G. J., Eds.; John Wiley & Sons, Ltd: Chichester, UK, 2019; ..
(45) Xu, J.; Wang, R.; Songtian, H.; Han, T.; Zhang, H.; Liu, J. Engineering Tin Dioxide Quantum Dots-Coated Iron Oxide Nanorods as Sulfur Host for Polysulfides-Immobile Lithium-Sulfur Battery. *J. Alloys Compd.* **2024**, *1009*, 176942.
(46) Li, B.; Sun, Z.; Zhao, Y.; Zhang, Z. Facile Synthesis of Three-Dimensional Carbon Nanotube/Fe3O4Microspheres as Sulfur Host for High Performance Lithium-Sulfur Batteries. *Mater. Lett.* **2019**, *255*, 126529.
(47) Du, Y.; Liu, Y.; Zhu, B.; Zhang, Q.; Tian, Z. N-Doped Carbon-Coated Halloysite Nanotubes as Cathode Materials for High-Performance Lithium-Sulfur Batteries. *J. Alloys Compd.* **2025**, *1010*, 177093.
(48) Wang, N.; Li, W.; Cao, G.; Duan, R.; Pei, J.; Luo, P.; Zhang, J.; Wang, J.; Li, X. Constructing Co/CoV2O6 Tandem Catalytic Heterostructure to Enhance Lithium Polysulfide Conversion in Lithium-Sulfur Batteries. *J. Alloys Compd.* **2024**, *980*, 173394.
(49) Fei, J.; Wang, Y.; Li, S.; Han, M.; Jia, H.; Liu, C. Preparation of CoO-CoP-CNT Heterogeneous Materials for Advanced Lithium-Sulfur Battery Cathode Electrode. *J. Alloys Compd.* **2023**, *966*, 171551.
(50) Li, X.; Shao, C.; Wang, X.; Wang, J.; Liu, G.; Yu, W.; Dong, X.; Wang, J. Preparation of Fe3O4/FexSy Heterostructures via Electrochemical Deposition Method and Their Enhanced Electrochemical Performance for Lithium-Sulfur Batteries. *Chem. Eng. J.* **2022**, *446*, 137267.
(51) Faheem, M.; Yin, X.; Shao, R.; Zhou, L.; Zeng, C.; Ahmad, N.; Tufail, M. K.; Yang, W. Efficient Polysulfide Conversion by Fe-N/C Active Sites Anchored in N, P- Doped Carbon for High-Performance Lithium-Sulfur Batteries. *J. Alloys Compd.* **2022**, *922*, 166132.
(52) Huang, Y.; Li, Z.; Zhu, T.; Gao, X.; Lv, X.; Ling, M.; Wan, Z.; Xia, Y. Ferromagnetic 1D-Fe 3 O 4 @C Microrods Boost Polysulfide Anchoring for Lithium−Sulfur Batteries. *ACS Appl. Energy Mater.* **2021**, *4*, 3921−3927.
(53) Lei, W.; Wang, X.; Zhang, Y.; Luo, Z.; Xia, P.; Zou, Y.; Ma, Z.; Pan, Y.; Lin, S. Facile Synthesis of Fe3C Nano-Particles/Porous Biochar Cathode Materials for Lithium Sulfur Battery. *J. Alloys Compd.* **2021**, *853*, 157024.
(54) Suriyakumar, S.; Rani, G. J.; Stephan, A. M. $Fe_3O_4$-Seated RGO−Sulfur Complex as a Potential Cathode Material for Lithium−Sulfur Batteries. *Ionics* **2020**, *26* (5), 2201−2210.


https://doi.org/10.1021/acs.jpcc.5c02606
J. Phys. Chem. C 2025, 129, 15507−15517